Intermittent energy dissipation by turbulent reconnection

H. S. Fu[1], A. Vaivads[2], Yu. V. Khotyaintsev[2], M. André[2], J. B. Cao[1], V. Olshevsky[3], J. P. Eastwood[4] & A. Retinò[5]

[1]School of Space and Environment, Beihang University, Beijing, China

[2]Swedish Institute of Space Physics, Uppsala, Sweden

[3]Center for Mathematical Plasma Astrophysics, KU Leuven, Leuven, Belgium

[4]The Blackett Laboratory, Imperial College London, London SW7 2AZ, United Kingdom

[5]Laboratoire de Physique des Plasmas, CNRS/Ecole Polytechnique/UPMC, Palaiseau, France

Key points:

- Strong current, turbulence, and energy dissipation at O-lines
- No current, turbulence, and energy dissipation at X-lines
- The current-driven turbulence at O-lines leads to dissipation

Abstract. Magnetic reconnection—the process responsible for many explosive phenomena in both nature and the laboratory—is efficient at dissipating magnetic energy into particle energy. To date, exactly how this dissipation happens remains unclear, owing to the scarcity of multi-point measurements of the 'diffusion region' at the sub-ion scale. Here we report such a measurement by Cluster—four spacecraft with separation of ⅕ ion scale. We discover numerous current filaments and magnetic nulls inside the diffusion region of magnetic reconnection, with the strongest currents appearing at spiral nulls (O-lines) and the separatrices. Inside each current filament, kinetic-scale turbulence is significantly increased, and the energy dissipation, $E' \cdot J$, is 100 times larger than the typical value. At the jet reversal point, where radial nulls (X-lines) are detected, the current, turbulence, and energy dissipations are surprisingly small. All these features clearly demonstrate that energy dissipation in magnetic reconnection occurs at O-lines but not X-lines.

1. Introduction

Magnetic reconnection in the solar corona [*Kopp and Pneuman,* 1976] and the Earth's magnetosphere [*Angelopoulos et al.*, 2008] is believed to occur in a small 'diffusion region' with scale of ion skin depth [*Øieroset et al.*, 2001]. Such a region generally follows the two-fluid picture [*Sonnerup*, 1979], but at its boundary the antiparallel-merging magnetic field lines may strongly fluctuate [*Lazarian and Vishniac,* 1999] and inside it fine structuring such as X-lines and O-lines typically appears (Fig. 1a). During reconnection, the magnetic field lines 'break' and 'reconnect', and a large amount of energy is released in terms of hard X-rays on the Sun [*Masuda et al.*, 1994] and energetic electrons in the magnetotail [*Hoshino et al.,* 2001; *Imada et al.,* 2007; *Huang et al.,* 2012; *Fu et al.,* 2013]. It is still a puzzle how so much magnetic energy is dissipated to particle energy in such a small region [*Birn et al.*, 2001]. The X-line is traditionally suggested as the main point where energy dissipation happens [*Shay et al.*, 2007; *Ji et al.*, 2008; *Yamada et al.*, 2014; *Burch et al.*, 2016], as two opposite plasma jets are always produced there. However, recent 3-D simulations indicate that O-lines may also be important [*Olshevsky et al.*, 2015]. So far, exactly where the energy dissipation happens has been unclear.

To reveal the energy dissipation during reconnection, identifying X-lines and O-lines should be the first step. This requires that (1) multiple spacecraft are located simultaneously inside the diffusion region and have sub-ion scale separations, and (2) a tool is available for reconstructing the fine structures around the spacecraft trajectories. The ESA four-spacecraft mission Cluster [*Escoubet et al.*, 2001] can readily satisfy the first criterion: In the autumn of 2003, Cluster detected a few magnetic reconnection events [*Eastwood et al.*, 2010] in the Earth's magnetotail, where the ion diffusion region has a

scale of 1000 km. In these events, Cluster had a separation of ~200 km, hence all satellites were located simultaneously inside the diffusion region. To meet the second criterion, we recently developed and tested a new method, i.e., the first-order Taylor expansion (FOTE) [*Fu et al.*, 2015; 2016]. We have used this method and the Cluster *in-situ* measurements in 2003 to reveal the energy dissipation during reconnection in this letter.

2. Observations

One of the reconnection events was detected by Cluster on 9 October 2003, at about 02:25 UT, when the spacecraft were located in the Earth's magnetotail at [-15.6, 9.2, 3.1] R_E (GSM coordinates). The general properties of this event have recently been analyzed [*Eastwood et al.*, 2009], and the local ion skin depth was identified as $d_i \approx 1000$ km. In this event, the four spacecraft, forming a regular tetrahedron with size of ~200 km, crossed the ion diffusion region from north to south (see the red arrow in Fig. 1a); they observed a reconnection current sheet, reflected in the reversal of the main magnetic field (B_L, Fig. 1c) from +20 nT (north edge of the current sheet, measured at 02:21:30 UT) to -20 nT (south edge of the current sheet, 02:27:30 UT). Inside this current sheet the average current density is about 10 nA/m^2 (see the horizontal blue bar in Fig. 2b). The four spacecraft measured very similar magnetic fields and flow velocities, indicating that the inter-spacecraft distance was small, and the interpolation/extrapolation of magnetic fields around the spacecraft tetrahedron is reliable [*Fu et al.*, 2015].

During the entire crossing, the B_N (Fig. 1e) and V_L (Fig. 1f) are generally negative. B_M (Fig. 1d) is negative in the north part of the current sheet (02:21:30 - 02:25:00 UT) but positive in the south part (02:25:00 - 02:27:30 UT); it exhibits a bipolar variation. These observations can be well described by the two-fluid model [*Sonnerup*, 1979;

60 *Øieroset et al.*, 2001; *Vaivads et al.*, 2004], with B_M corresponding to the Hall magnetic
61 field (see Fig. 1a). The average value of B_M is close to zero inside the diffusion region,
62 meaning that there is virtually no guide field in this reconnection event. The multiple
63 fluctuations in B_L (Fig. 1c) follow a -5/3 power law in the inertial range [*Eastwood et al.*,
64 2009], suggesting that the magnetic reconnection is turbulent [*Lazarian and Vishniac*,
65 1999; *Daughton et al.*, 2011; *Karimabadi et al.*, 2013].

66 We notice that sometimes the magnetic field strength |**B**| approaches zero (Fig. 1b),
67 indicating the potential existence of magnetic nulls [*Lau and Finn*, 1990; *Parnell et al.*,
68 1996; *Priest and Forbes*, 2000] inside the diffusion region. Using the FOTE method [*Fu*
69 *et al.*, 2015; 2016], we search for magnetic nulls around the spacecraft trajectory, and
70 also analyze the topological property of each null (The accuracy of FOTE, as well as a
71 comparison with previous methods, have been well discussed by *Fu et al.* [2015]). Fig. 2a
72 shows all the nulls with distance less than 1000 km (1 d_i) from the spacecraft. Properties
73 of the nulls lying less than 500 km (0.5 d_i, see the horizontal grey line) from the
74 spacecraft are presented in Fig. 3, and also labeled at the top of Fig. 2a. We see that there
75 are many magnetic nulls around the spacecraft. Some of the nulls (for example, the null at
76 02:25:04.45 UT) are only 50 km (~2 d_e) away from one of the spacecraft. During the
77 entire crossing of the diffusion region, most of the magnetic nulls are found to be of the
78 spiral-type (A_s, B_s, O) [*Parnell et al.*, 1996]. Only two nulls belong to radial-type (A, B,
79 X) [*Parnell et al.*, 1996]; these two nulls were detected at 02:24:27 UT (Fig. 3f) and
80 02:25:05 UT (Fig. 3j), corresponding to the flow stagnation or maybe the flow reversal
81 (see Fig. 1f). Such a correspondence between X-null and flow reversal implies that the
82 magnetic field lines quite possibly ‘break’ there.

Using the Curlometer technique [*Dunlop et al.*, 2002], we calculate the current density inside the diffusion region, and find many current filaments there (Fig. 2b). These current filaments, having scales larger than the spacecraft separation (see Supplementary Information S6), show a rather good correlation with the spiral nulls: when the spacecraft is close to a spiral null, the current becomes strong; when the spacecraft move away from a spiral null, the current becomes weak. We mark the strongest current filaments (>30 nA/m^2) with numbers 1-5. At the fourth filament (02:26:18 UT), the current is strong but there is no spiral null; this current filament may correspond to a separatrix, where a field-aligned current usually exists [*Khotyaintsev et al.*, 2006]. At the X-nulls, the current is very weak or even disappears. For instance, at 02:25:05 UT (blue vertical dashed line) Cluster detected an X-null, where the current decreased to 0.5 nA/m^2, much smaller than the average value, 10 nA/m^2. Around 02:24:26 UT, Cluster quickly encountered first a spiral null then a radial null (Fig. 3f), and simultaneously, the current changed from strong to weak (see Supplementary Information S1). The direction of current filaments 1 and 3 are shown in Fig. 4a-4b, together with the topology of the magnetic field. These two currents are nearly perpendicular to the magnetic field (along the spine of the null [*Parnell et al.*, 1996], see the green arrow). The fan-aligned current suggested in previous models [*Pontin et al.*, 2005] is not seen at these two nulls. Near the separatrix (02:26:18 and 02:27:25 UT), we find the current is indeed parallel to the magnetic field (see Supplementary Information S2), as expected.

The magnetic field topologies in Fig. 4 are reconstructed using the FOTE method (see *Fu et al.* [2015] for the accuracy of these reconstructions). We find that the reconstructed topologies are consistent with theoretical models [*Lau and Finn*, 1990; *Parnell et al.*,

106 1996; *Priest and Forbes*, 2000]. In Fig. 4c, the 'radial' feature of the null at 02:25:05 UT
107 is clear. Looking along the direction (e_1, e_2, 0), we find this radial null becomes an X-line
108 structure (Fig. 4f), with an angle of 78° between the two separatrix-lines. In Fig. 4a-4b,
109 the 'spiral' feature of the null is clear as well. When we look along the direction (e_1, 0, 0),
110 these spiral nulls become magnetic islands or magnetic flux ropes (Fig. 4d-4e).

111 The current can significantly modulate the kinetic-scale turbulence [*Che et al.*, 2011].
112 In Fig. 2c, we see that when the current is large (for example, current filaments 1-5), the
113 turbulence is strong; when the current is small (for example, before 02:22:00 UT or after
114 02:27:30 UT), the turbulence is weak. We quantitively compare the turbulence intensity
115 at current filaments 1-5 and X-null with that averaged during 02:20 - 02:30 UT, i.e., in
116 the whole reconnection current sheet (Fig. 2e). We find that the turbulence intensity
117 inside each filament is significantly larger than the average value (Fig. 2e). At the X-null
118 (blue vertical dashed line), where flow speed touches zero or quite possibly is reversed,
119 the turbulence almost disappears. Such a correlation between kinetic-scale turbulence and
120 current is also found in the electric field data (see Supplementary Information S3); it
121 indicates that the turbulence is current-driven and may cause scattering of particles,
122 which then leads to energy dissipation [*Zenitani et al.*, 2011].

123 Fig. 2d shows energy dissipation rate during the whole period. This energy
124 dissipation becomes spiky in the outflow region and apparently happens at spiral nulls,
125 where both the current and kinetic-scale turbulence are very strong. During the whole
126 period, the dissipation is generally positive ($\mathbf{E'}\cdot\mathbf{j} > 0$), meaning that magnetic energy is
127 being dissipated and transformed into particle energy. At 02:24:32.42 UT (current
128 filament 3), the energy dissipation reaches 300 pW/m^3, more than thirty times larger than

129 the average value, 10 pW/m^3, which is estimated from the background current density
130 ($j_M \approx 10$ nA/m^2) and electric field ($E_M \approx 1$ mV/m) inside the reconnection current sheet
131 (02:20 - 02:30 UT); it is also one hundred times larger than the typical energy dissipation
132 rate in the plasma sheet [*Hamrin et al.*, 2011] and comparable to that at the downstream
133 dipolarization fronts [*Angelopoulos et al.*, 2013].

134 We perform a 3-D kinetic simulation (see Supplementary Information S5) to
135 examine whether these spacecraft observations are also found in the simulations. In Fig.
136 2f, the simulation snapshot shows that the currents are generally perpendicular to the
137 magnetic field near spiral nulls. Almost all the energy dissipation occurs at spiral nulls
138 (O-lines), with the positive dissipation ($\mathbf{E'}\cdot\mathbf{j} > 0$) more dominant in the whole simulation box
139 than the negative ($\mathbf{E'}\cdot\mathbf{j} < 0$). At radial nulls (X-lines), both the current and energy dissipation
140 are absent. Such intermittent energy dissipation is also found in other kinetic simulations
141 [*Pritchett and Mozer*, 2009; *Wan et al.*, 2015; *Pritchett*, 2016]; it significantly diminishes
142 the importance of X-lines and therefore supports the Cluster observations (Fig. 2d).

143 **3. Conclusions**

144 Magnetic reconnection is crucial for interpreting many explosive phenomena in the
145 Sun (e.g., solar flares) and the Earth's magnetosphere (e.g., substorms). Using Cluster
146 measurements and iPIC3D simulations we have revealed that energy dissipation during
147 magnetic reconnection is spiky from turbulence and occurs primarily at O-lines. We find
148 no significant dissipation at the X-lines, which challenges the traditional belief of
149 magnetic reconnection process. These findings are crucial, in particular, for
150 understanding the intrinsic nature of magnetic reconnection.

151

References

Angelopoulos, V., et al. (2008), Tail reconnection triggering substorm onset, *Science,* **321**, 931-935.

Angelopoulos, V., et al. (2013), Electromagnetic energy conversion at reconnection fronts, *Science,* **341**, 1478.

Birn, J., et al. (2001), Geospace Environment Modeling (GEM) magnetic reconnection challenge, *J. Geophys. Res.,* **106**, 3715–3720.

Burch, J. L. et al. (2016), Electron-scale measurements of magnetic reconnection in space, *Science*, **352**, aaf2939.

Che, H., J. F. Drake, and M. A. Swisdak (2011), current filamentation mechanism for breaking magnetic field lines during reconnection, *Nature,* **474**, 184–187.

Daughton, W., et al. (2011), Role of electron physics in the development of turbulent magnetic reconnection in collisionless plasmas, *Nat. Phys*., **7**, 539–542.

Dunlop, M. W., et al. (2002), Four-point Cluster application of magnetic field analysis tools: The Curlometer, *J. Geophys. Res*., **107**, 1384.

Eastwood, J. P., et al. (2009), Observations of turbulence generated by magnetic reconnection, *Phys. Rev. Lett*., **102**, 035001.

Eastwood, J. P., T. D. Phan, M. Øieroset, and M. A. Shay (2010), Average properties of the magnetic reconnection ion diffusion region in the Earth's magnetotail: The 2001–2005 Cluster observations and comparison with simulations, *J. Geophys. Res.*, **115**, A08215.

Escoubet, C. P., M. Fehringer, and M. Goldstein (2001), Introduction: The Cluster

173 mission, *Ann. Geophys.*, **19**, 1197–1200.

174 Fu, H. S., Y. V. Khotyaintsev, A. Vaivads, A. Retinò, and M. André (2013), Energetic
175 electron acceleration by unsteady magnetic reconnection, *Nat. Phys.*, **9**, 426–430.

176 Fu, H. S., et al. (2015), How to find magnetic nulls and reconstruct field topology with
177 MMS data?, *J. Geophys. Res. Space Physics,* **120**, 3758–3782.

178 Fu, H. S., et al. (2016), Identifying magnetic reconnection events using the FOTE
179 method, *J. Geophys. Res. Space Physics,* **121**, 1263–1272.

180 Hamrin, M., et al. (2011), Energy conversion regions as observed by Cluster in the
181 plasma sheet, *J. Geophys. Res*., **116**, A00K08.

182 Hoshino, M., T. Mukai, T. Terasawa, and I. Shinohara (2001), Suprathermal electron
183 acceleration in magnetic reconnection, *J. Geophys. Res.*, **106**, 25979–25997.

184 Huang, S. Y., et al. (2012), Electron acceleration in the reconnection diffusion region:
185 Cluster observations, *Geophys. Res. Lett.*, **39**, L11103.

186 Imada, S., et al. (2007), Energetic electron acceleration in the downstream reconnection
187 outflow region, *J. Geophys. Res.*, **112**, A03202.

188 Ji, H., et al. (2008), New insights into dissipation in the electron layer during magnetic
189 reconnection, *Geophys. Res. Lett.,* **35**, L13106.

190 Karimabadi, H., et al. (2013), Recent evolution in the theory of magnetic reconnection
191 and its connection with turbulence, *Space Sci. Rev.,* **178**, 307–323.

192 Khotyaintsev, Y. V., et al. (2006), Formation of inner structure of a reconnection
193 separatrix region, *Phys. Rev. Lett*., **97**, 205003.

194 Kopp, R. A., and G. W. Pneuman (1976), Magnetic reconnection in the corona and the
195 loop prominence phenomenon, *Sol. Phys.*, **50**, 85–98.

196 Lau, Y.-T., and J. Finn (1990), Three-dimensional kinematic reconnection in the presence
197 of field nulls and closed field lines, *Astrophys. J.,* **350**, 672–691.

198 Lazarian, A., and E. T. Vishniac (1999), Reconnection in a weakly stochastic field,
199 *Astrophys. J.*, **517**, 700-718.

200 Masuda, S., et al. (1994), A loop-top hard X-ray source in a compact solar flare as
201 evidence for magnetic reconnection, *Nature,* **371**, 495-497.

202 Øieroset, M., et al. (2001), In situ detection of collisionless reconnection in the Earth's
203 magnetotail, *Nature,* **412**, 414-417.

204 Olshevsky, V., et al. (2015), Energy dissipation in magnetic null points at kinetic scales,
205 *Astrophys. J.,* **807**, 155.

206 Parnell, C. E., et al. (1996), The structure of three-dimensional magnetic neutral points,
207 *Phys. Plasmas,* **3**, 759–770.

208 Pontin, D. I., G. Hornig, and E. R. Priest (2005), Kinematic reconnection at a magnetic
209 null point: Fan-aligned current, *Geophys. Astrophys. Fluid Dyn.,* **99**, 77–93.

210 Priest, E. R., and T. G. Forbes (2000), Magnetic Reconnection: MHD Theory and
211 Applications*, Cambridge Univ. Press*.

212 Pritchett, P. L., and F. S. Mozer (2009), The magnetic field reconnection site and
213 dissipation region, *Phys. Plasmas*, **16**, 080702.

214 Pritchett, P. L. (2016), Three-dimensional structure and kinetic features of reconnection

exhaust jets. *J. Geophys. Res. Space Physics* **121**, 214–226.

Shay, M. A., J. F. Drake, and M. Swisdak (2007), Two-scale structure of the electron dissipation region during collisionless magnetic reconnection, *Phys. Rev. Lett.,* **99**, 155002.

Sonnerup, B. U. Ö. (1979), Magnetic field reconnection, in Solar System Plasma Physics, vol. 3, Solar System Plasma Processes, edited by L. T. Lanzerotti, C. F. Kennel, and E. N. Parker, pp. 45–108, North-Holland, New York.

Vaivads, A., et al. (2004), Structure of the magnetic reconnection diffusion region from four-spacecraft observations, *Phys. Rev. Lett*., **93**, 105001.

Wan, M., W. Matthaeus, V. Roytershteyn, H. Karimabadi, T. Parashar, P. Wu, and M. Shay (2015), Intermittent dissipation and heating in 3D kinetic plasma turbulence, *Phys. Rev. Lett.*, **114**, 175002.

Yamada, M., et al. (2014), Conversion of magnetic energy in the magnetic reconnection layer of a laboratory plasma, *Nat. Commun.,* **5**, 4774.

Zenitani, S., et al. (2011), New measure of the dissipation region in collisionless magnetic reconnection, *Phys. Rev. Lett.,* **106**, 195003.

Acknowledgements. We thank Cluster Science Archive (http://www.cosmos.esa.int/web/csa) for providing the data for this study. The fruitful discussions with S. Y. Huang at Wuhan University are appreciated. This research was supported by NSFC grants 41574153, 41431071, 41404133, and the Swedish Research Council. J.P.E. was supported by STFC(UK) grants ST/K001051/1 and ST/N000692/1.

Figure captions

Figure 1. Reconnection diffusion region detected by Cluster in the Earth's magnetotail. Data are shown in a current sheet coordinate system LMN: L points earthward and contains the main magnetic field reversal, N is normal to the current sheet, and [L, M, N] is a right-handed triple. Relative to geocentric solar magnetospheric (GSM) coordinates, L=(0.895, -0.441, 0.068), M=(0.445, 0.892, -0.072), N=(-0.029, 0.094, 0.994). (a) A schematic showing the ion diffusion region of magnetic reconnection (modified from *Karimabadi et al.* [2013, Fig. 7]). The fluctuating boundaries at top and bottom, and the fine structures inside the diffusion region, indicate that the reconnection is turbulent. However, the two-fluid pattern can still be recognized: Hall electric current (white dashed line), caused by the separate motion of ions and electrons at the ion inertial scale, and the associated quadrupolar structure of the out-of-plane magnetic field, both exist. Cluster passed the tailward side of the diffusion region from north to south (vertical red arrow), but occasionally touched the X-null, where the flow speed is reversed. As the Cluster separation (200 km) is much smaller than the ion diffusion region (1000 km), we show the Cluster trajectory as a single arrow. (b) The magnetic field strength. (c) The magnetic field B_L component, showing the main magnetic field reversal. (d) The magnetic field B_M component, representing the Hall magnetic field. (e) The magnetic field B_N component. (f) The jet speed V_L component. In Figs. 1b-1f, the measurements by Cluster 1-4 are shown, respectively, in black, red, green, and blue. Magnetic field data (b-e) are provided by FGM, while jet speed data (f) are provided by CIS-HIA. FGM and CIS-HIA are two instruments onboard Cluster satellites. On Cluster 2 and 4, the CIS-HIA measurements are unavailable. The two X-nulls in Fig. 1f correspond to those in Figs. 3f and 3j.

Figure 2. Fine structures and energy dissipations in reconnection diffusion region. (a) The null-spacecraft distance resolved using the FOTE method, with the null types labeled at the top. The black, red, green, and blue lines represent the distances between Cluster 1-4 and magnetic nulls, respectively. The nulls at >1000 km from the spacecraft are not shown, while the nulls at <500 km (horizontal grey bar) from the spacecraft are examined in detail in Fig. 3. d_i and d_e denotes the local ion and electron skin depth, respectively. (b) The current density derived from Curlometer with its reliability verified in Supplementary Information S6. The horizontal blue bar indicates the average current density of the reconnection current sheet; the numbers 1-5 mark five strong current filaments. If the spacecraft is far from a null (e.g., δR>500 km), the Curlometer-derived current cannot represent the situation at null point. (c) The kinetic-scale turbulence of B_Z measured by STAFF. Only the magnetic field turbulence is shown; the electric field turbulence is presented in Supplementary Information S3. The black line in Fig. 2c is copied from Fig. 2b (with no units), to show the modulation of kinetic-scale turbulence by current filaments. (d) The energy dissipation rate $\mathbf{E'}\cdot\mathbf{j}$. The electric field used here is the average of the C2 and C4 measurements. The electric field component along the spacecraft spin axis is obtained from the condition $\mathbf{E}\cdot\mathbf{B} = 0$. The parallel electric field does not play a dominant role for energy dissipation, as the strongest currents are predominantly perpendicular ($j_{//} \approx 0$) near spiral nulls (see the spacecraft measurements in Supplementary Information S2 and the 3-D kinetic simulations in Fig. 2f). This means that $\mathbf{E'}\cdot\mathbf{j} = E_{\perp}'\cdot j_{\perp} + E_{//}\cdot j_{//} \approx E_{\perp}'\cdot j_{\perp}$. There are some data gaps in Fig. 2d, because during these periods the magnetic field vector was close to the spin plane of spacecraft. (e) The power spectral density (PSD) of B_Z and Ey, for examining the kinetic-scale turbulence

283 inside each current filament and at the X-line. The grey dotted line is an average value
284 from 02:20 to 02:30 UT. (f) The 3-D kinetic simulation of energy dissipation at different
285 types of magnetic nulls (see Supplementary Information S5 for details). The right top
286 color bar specifies the A_s (origin), B_s (red), A (cyan), and B (blue) nulls in the simulation
287 box, while the right bottom color bar presents the energy dissipation around nulls. Due to
288 the view angle of the 3-D simulation box, the nulls do not have same size. In Fig. 2f, the
289 red curves and black arrows show the magnetic field and electron currents, respectively.

290

291 **Figure 3.** Properties of magnetic nulls inside diffusion region. The matrix $\delta\mathbf{B}$ from four-
292 spacecraft measurements has three eigenvectors, $\mathbf{e}_1$, $\mathbf{e}_2$, $\mathbf{e}_3$, and correspondingly three
293 eigenvalues, λ_1, λ_2, λ_3. These three eigenvalues have a sum of zero, meaning that either
294 all of them are real or one is real while the two others are conjugate complex. If all the
295 eigenvalues are real, the magnetic null is of radial type, which includes A- and B-type.
296 The A-null has one positive and two negative eigenvalues (+, -, -), while the B-null has
297 two positive and one negative eigenvalues (+, +, -). If one eigenvalue is real while the
298 two others are conjugate complex, the magnetic null is of spiral type, which includes A_s-
299 and B_s-type. The A_s-null has positive real eigenvalue (+, +i, -i), while the B_s-null has
300 negative real eigenvalue (-, +i, -i). A, B, A_s, and B_s are all the null types in 3-D
301 reconnection. They can, however, degenerate into 2-D X-lines and O-lines in some
302 conditions [*Fu et al.,* 2015]. Specifically, the A-null and B-null will degenerate into X-
303 line, if the absolute value of one eigenvalue is significantly smaller than the two others,
304 i.e., $\min(|\lambda|) < ¼\cdot\max(|\lambda|)$. The A_s-null and B_s-null will degenerate into O-line, if the real
305 part of the eigenvalue is significantly smaller than the imaginary part, $\max(|\mathrm{Real}(\lambda)|) <$
306 $¼\cdot\min(|\mathrm{Imag}(\lambda)|)$. Regarding the X-line and O-line, the eigenvalues should approximately

have signs (0, +, -) and (0, +i, -i), respectively. The O-line is usually identified as a magnetic island (without guide field) or flux rope (with guide field). If the relation of the three eigenvalues belong to none of the six categories above (usually due to large uncertainties), we cannot identify the null type, and therefore label it as "unknown" using the symbol "□". In Fig. 3, δR represents the minimum distance between the null and Cluster 1-4. The types of these nulls have been labeled at the top of Fig. 2a. The uncertainties of these null-type identifications are shown in Supplementary Information S4, while the eigenvalues used for identifications are shown in Supplementary Information S7.

Figure 4. Topology of magnetic nulls and the associated current filaments. Data are shown in the eigenvector coordinate system (e_1, e_2, e_3). Reconstructions are from the FOTE method. (a) The 3-D magnetic field topology around Cluster at 02:22:14.66 UT; it corresponds to the first strong current filament in Fig. 2b. (d) A 2-D view, along the direction (e_1, 0, 0), of this topology. (b) The 3-D magnetic field topology around Cluster at 02:24:32.42 UT, corresponding to the third strong current filament in Fig. 2b. (e) A 2-D view, along the direction (e_1, 0, 0), of this topology. (c) The 3-D magnetic field topology around Cluster at 02:25:04.45 UT, corresponding to the vertical blue line in Fig. 2b, and also the flow stagnation in Fig. 1f. (f) A 2-D view, along the direction (e_1, e_2, 0), of this topology. The colour represents the magnetic field strength |**B**|, while the blue arrows show the magnetic field direction. In Figs. 4a-4b, the green arrows denote the direction of current filaments; while in Fig. 4c, the current is almost zero. The magnetic field topology indicates a B_s-null in Fig. 4a, but an A_s-null in Fig. 4b. In Fig. 4c, it indicates an A-null.

Figures

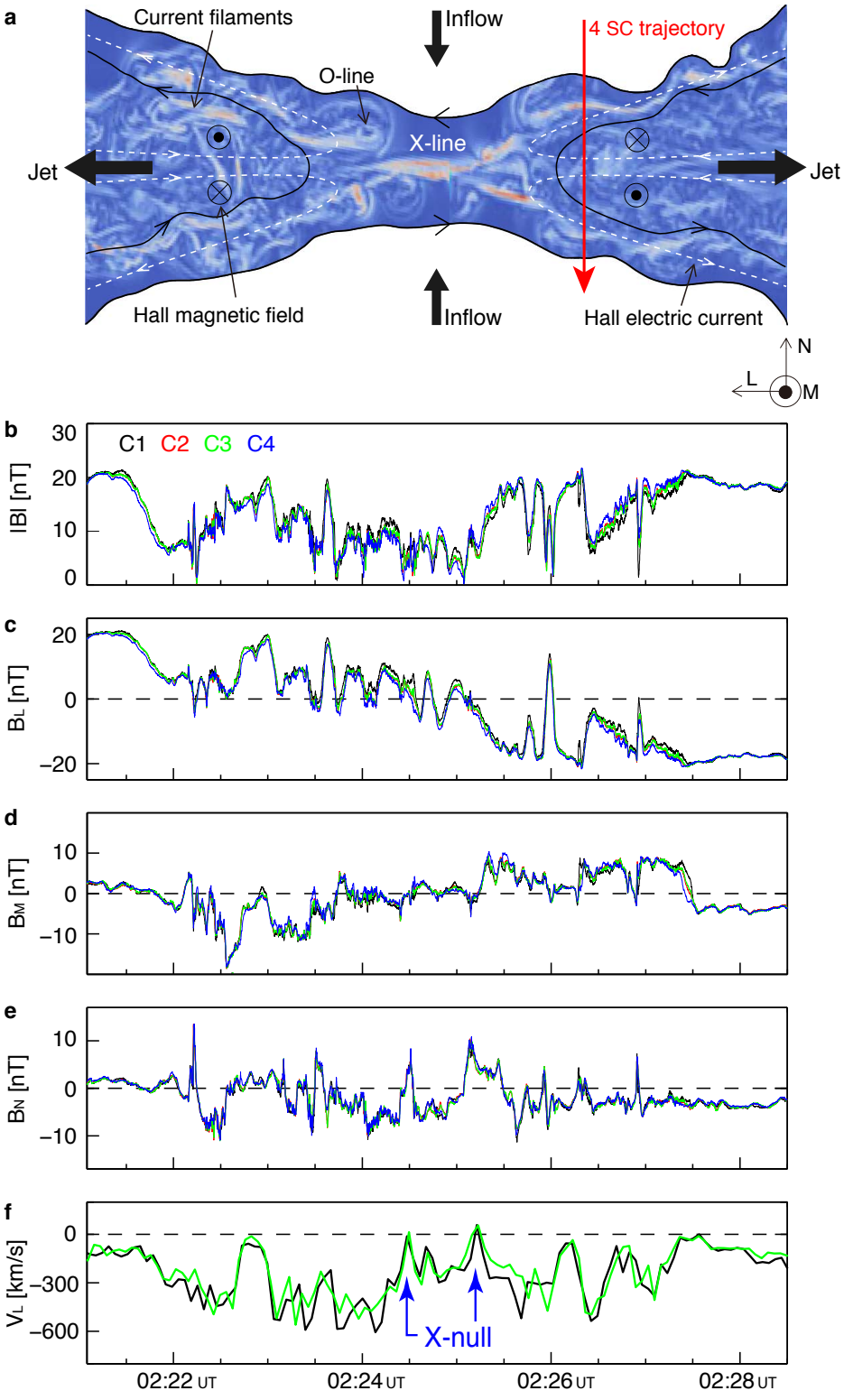

Fig. 1

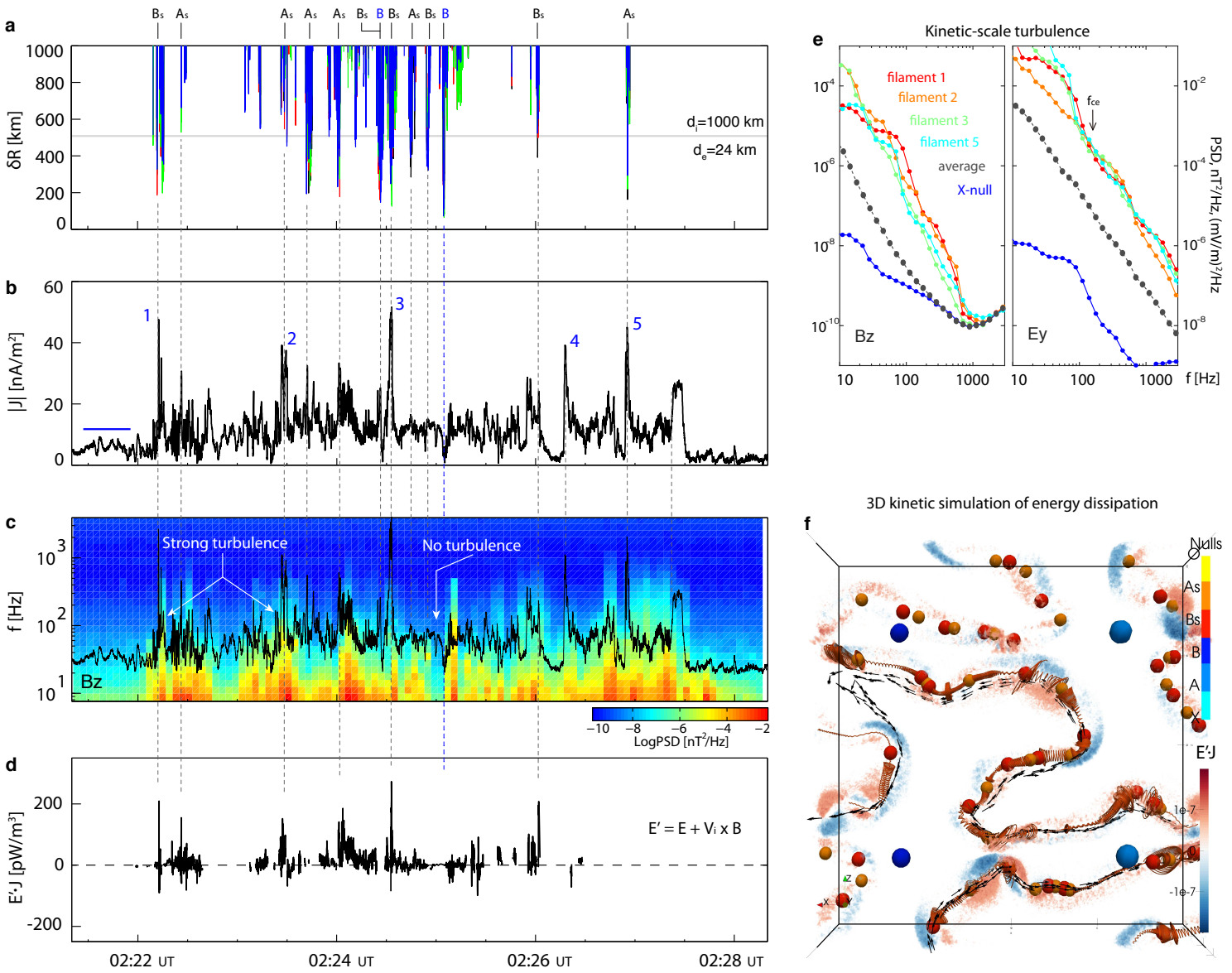
a
δR [km]
d_i=1000 km
d_e=24 km
b
|J| [nA/m²]
c
f [Hz]
Strong turbulence
No turbulence
Bz
LogPSD [nT²/Hz]
d
E'·J [pW/m³]
E' = E + Vi x B
02:22 UT
02:24 UT
02:26 UT
02:28 UT
e
Kinetic-scale turbulence
filament 1
filament 2
filament 3
filament 5
average
X-null
Bz
Ey
f_ce
PSD, nT²/Hz, (mV/m)²/Hz
f [Hz]
f
3D kinetic simulation of energy dissipation
Nulls
As
Bs
B
A
E'·J

Fig. 2

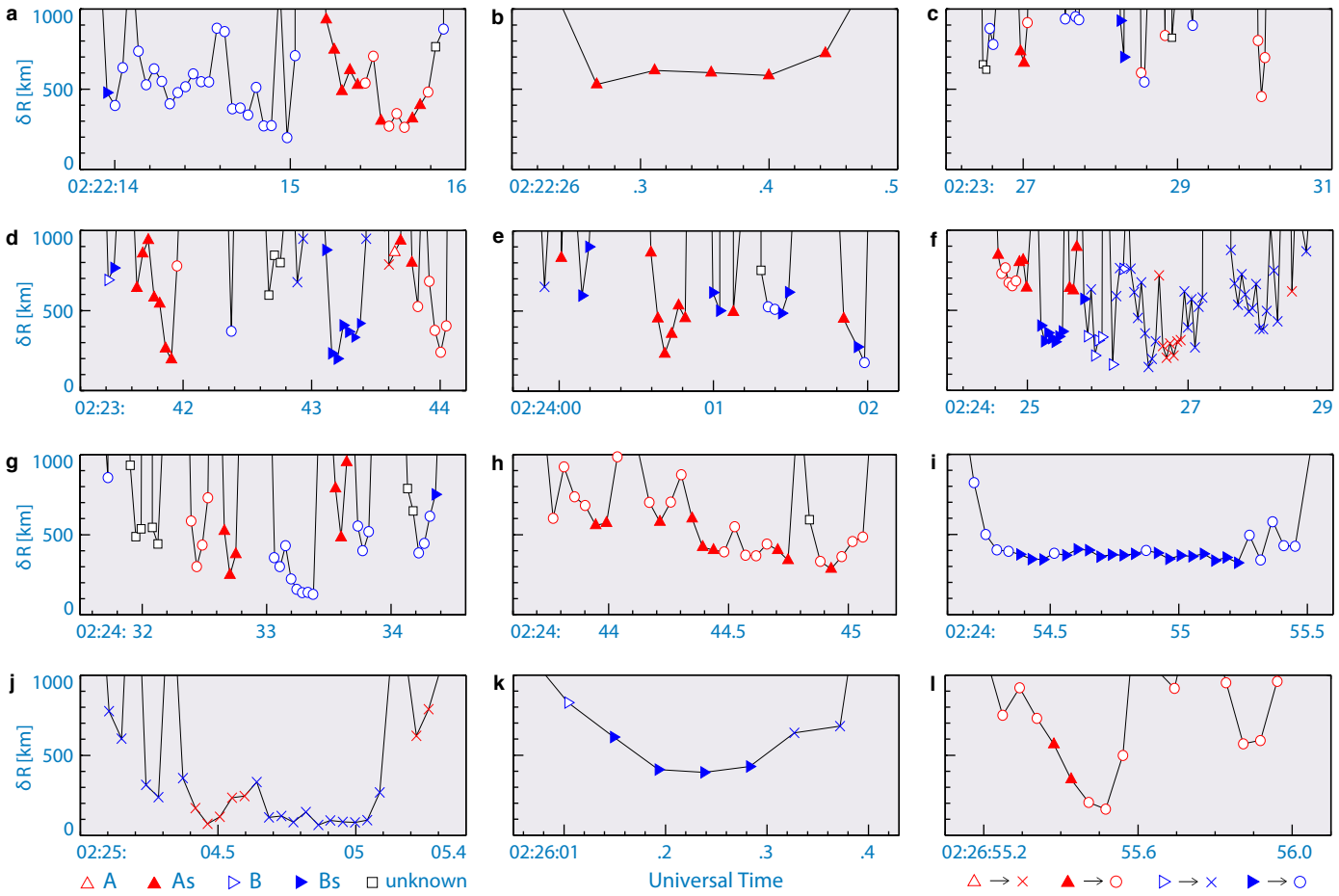
a
b
c
d
e
f
g
h
i
j
k
l
δR [km]
1000
500
0
02:22:14
15
16
02:22:26
.3
.4
.5
02:23:
27
29
31
42
43
44
02:24:00
01
02
02:24:
25
27
29
32
33
34
44
44.5
45
54.5
55
55.5
02:25:
04.5
05
05.4
02:26:01
.2
.3
.4
02:26:55.2
55.6
56.0
A
As
B
Bs
unknown
Universal Time

Fig. 3

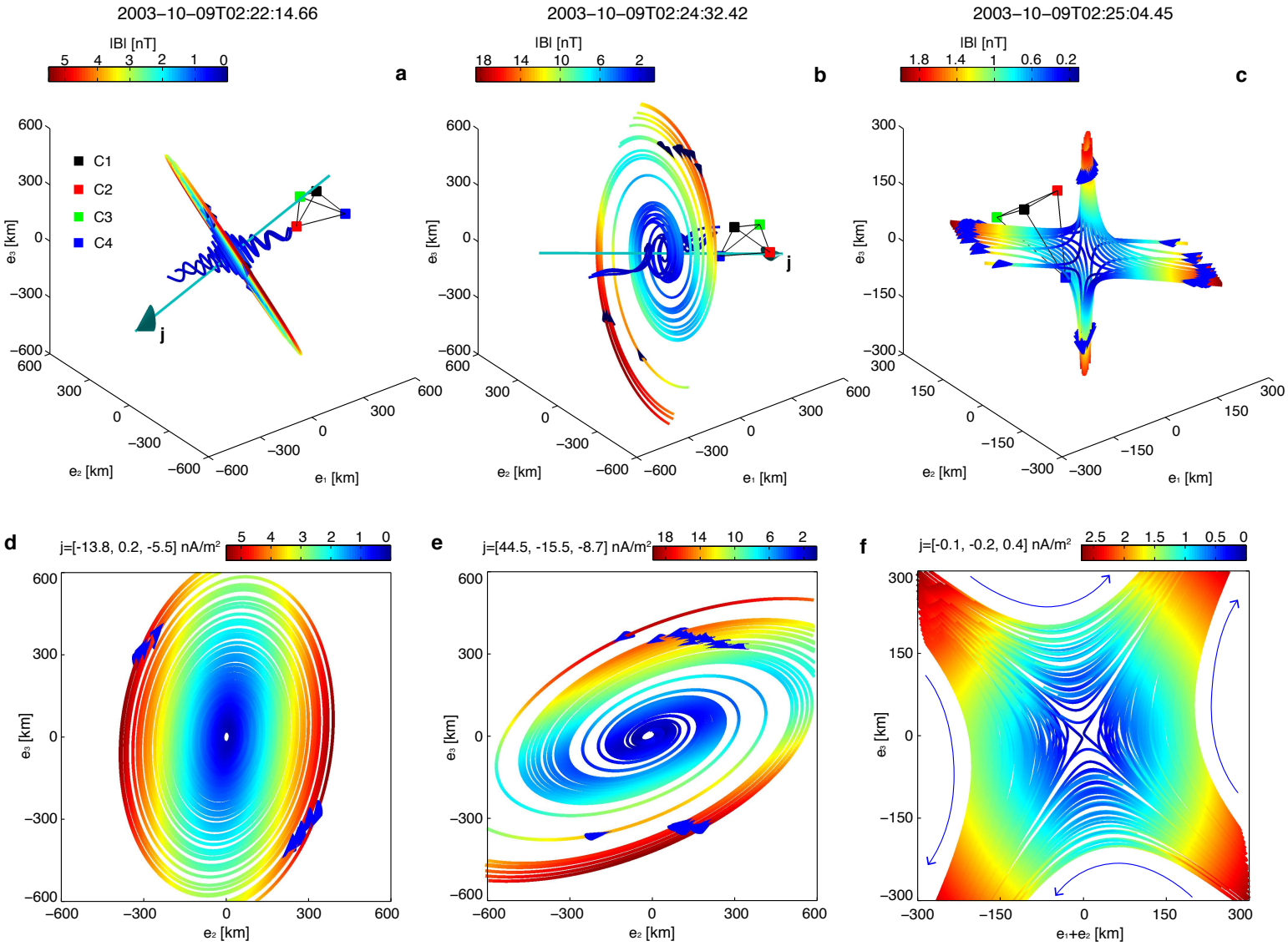
2003−10−09T02:22:14.66
2003−10−09T02:24:32.42
2003−10−09T02:25:04.45
|B| [nT]
a
b
c
C1
C2
C3
C4
j
e₁ [km]
e₂ [km]
e₃ [km]
d
e
f
j=[-13.8, 0.2, -5.5] nA/m²
j=[44.5, -15.5, -8.7] nA/m²
j=[-0.1, -0.2, 0.4] nA/m²
e₁+e₂ [km]

Fig. 4